

Moment evolution equations and moment matching for stochastic image EPDiff

Alexander Mangulad Christgau · Alexis Arnaudon · Stefan Sommer

Received: date / Accepted: date

Abstract Models of stochastic image deformation allow study of time-continuous stochastic effects transforming images by deforming the image domain. Applications include longitudinal medical image analysis with both population trends and random subject specific variation. Focusing on a stochastic extension of the LDDMM models with evolutions governed by a stochastic EPDiff equation, we use moment approximations of the corresponding Itô diffusion to construct estimators for statistical inference in the full stochastic model. We show that this approach, when efficiently implemented with automatic differentiation tools, can successfully estimate parameters encoding the spatial correlation of the noise fields on the image.

Keywords Stochastic shape analysis · Image registration · LDDMM · Stochastic differential equations

1 Introduction

The Large deformation diffeomorphic metric mapping (LDDMM) framework was developed with the intention to model deformations of images and shapes, driven by applications in fields including medical imaging and biology. LDDMM models shape and image evolution

as a gradual process induced by time-continuous paths ϕ_t of deformations. The model is therefore naturally applicable to longitudinal studies to investigate shape evolution of human organs during child development, natural aging or disease processes.

To model subject-specific deviations from a population-mean deformation, it is natural to incorporate noise into the LDDMM framework. One approach is to consider random variation in the initial velocity $u_0 = \partial_t \phi_t|_{t=0}$ as in e.g. the random orbit model [11, 15] or Bayesian principal geodesic analysis [19]. Instead of assuming that the entire variation is the result of a random event at the beginning, [16, 17, 10, 2] propose to include time-continuous noise. A general framework for stochastic shape analysis with the variability incorporated as random variation over the entire evolution is proposed in [2] by using *noise fields* $\sigma_1, \dots, \sigma_p$, to perturb the deformation ϕ_t , thus creating the stochastic flow. The framework and examples of its effect on medical images is illustrated in Figure 1. Estimation of noise in this framework was considered in [2] for landmark data. Noise estimation for images is inherently more difficult due to the infinite dimensional nature of the observations and the non-linear coupling between deformation and image.

In this paper, we develop a new approach for estimation of noise in the stochastic framework from image data. Specifically, we derive moment equations of the stochastic evolution in image and momentum space, and we implement these in a modern image registration framework allowing automatic differentiation of the moment equations and subsequent optimization. Using the derived estimators, we perform simulation studies demonstrating the ability of the scheme to estimate unknown parameters of the stochastic noise.

Alexander Mangulad Christgau
Department of Mathematical Sciences, University of Copenhagen, Denmark
E-mail: amc@math.ku.dk

Alexis Arnaudon
Department of Mathematics, Imperial College, London, UK.
E-mail: alexis.arnaudon@imperial.ac.uk

Stefan Sommer
Department of Computer Science, University of Copenhagen, Denmark
E-mail: sommer@di.ku.dk

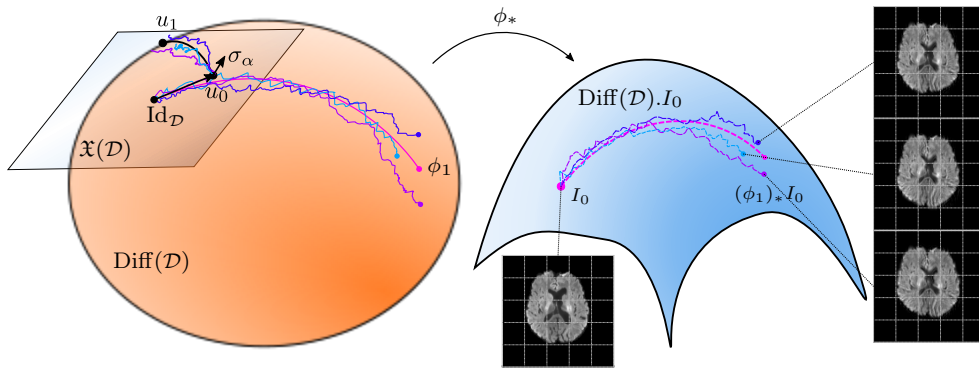


Fig. 1: (left) Illustrations of some random sample paths on the diffeomorphism group $\text{Diff}(\mathcal{D})$ induced by a random motion of vector fields governed by the stochastic EPDiff equation (9). (center) Starting with an image I_0 , e.g. a brain MR-slice, each path of diffeomorphisms deforms the image by the pushforward-action. (right) Some resulting samples of the endpoint image $(\phi_1)_* I_0 = I_0 \circ \phi_1^{-1}$ are shown on the right.

The paper builds on initial steps for noise estimation from image deformation models using strings [1] and the Fourier space moment approximations in the preprint [9]. The paper thus presents the following contributions:

1. We derive approximated first-order moment equations for the stochastic EPDiff and advection equations of images (SEFDA).
2. We construct estimators based on matching of first-order moments of the images.
3. We show how the scheme can be implemented in a modern image registration framework allowing automatic differentiation through the moment equations.
4. We demonstrate the ability of the methods to estimate noise fields with simulated data, both in a correctly specified model and with misspecification.

1.1 Plan of Paper

In Section 2, we briefly describe the LDDMM framework and its stochastic generalization from [2] in the special case of image deformation. In Section 3, we first derive the moment equations for the momentum and image flow (m_t, I_t) . We then use approximations of these to define a new procedure for parameter estimation in the stochastic framework based on the method of moments. In Section 4, we discuss the numerical implementation which is used to investigate the moment estimators with simulation studies. In Section 5, the results of the simulation studies are presented and discussed. We end the paper with concluding remarks.

2 Background

We briefly introduce the LDDMM framework in the context of image registration. A detailed treatment can be found in [18], and, with a perspective from geometric mechanics, [3, 4].

The main objects of interest are (grayscale) images, which are given as maps $\mathcal{D} \rightarrow \mathbb{R}$ defined on an image domain $\mathcal{D} \subseteq \mathbb{R}^d$, and the space of images is denoted by $\mathcal{I}(\mathcal{D})$. Our prototypical example of an image domain is $\mathcal{D} = (0, 1)^2$, although the theory naturally extends to general domains including 3D-images. A deformation of images is modeled by a path of diffeomorphisms $\phi = (\phi_t)_{t \in [0, 1]} \subset \text{Diff}(\mathcal{D})$ starting at the identity map $\phi_0 = \text{Id}_{\mathcal{D}}$, where $\text{Diff}(\mathcal{D})$ denotes the group of diffeomorphisms on \mathcal{D} . A deformation is further assumed to be generated as the flow of a time-dependent vector field $u = (u_t)_{t \in [0, 1]} \subset \mathfrak{X}(\mathcal{D}) := C^\infty(\mathcal{D}, \mathbb{R}^d)$ via the *reconstruction equation*

$$\partial_t \phi_t = u_t \circ \phi_t, \quad t \in [0, 1]. \quad (1)$$

This equation and every following equation of mappings can be interpreted by pointwise evaluation for each point in \mathcal{D} . A path of diffeomorphisms induces a path of images I_t by the pushforward-action $(\phi_t)_* I = I \circ \phi_t^{-1} =: I_t$. Given a *source image* I_0 and a *target image* T we consider the energy functional E given by

$$E(u) = \frac{1}{2} \int_0^1 \|u_t\|_{\mathfrak{X}(\mathcal{D})}^2 dt + \frac{1}{2\lambda^2} \|I_0 \circ \phi_1^{-1} - T\|_{L^2(\mathcal{D})}^2, \quad (2)$$

where $\lambda > 0$ is a given trade-off parameter and where the norm on $\mathfrak{X}(\mathcal{D})$ is assumed to be of the form $\|u\|_{\mathfrak{X}(\mathcal{D})}^2 = \langle u, Lu \rangle_{L^2(\mathcal{D}, \mathbb{R}^3)}$ for some positive self-adjoint operator L . The first term is the *kinetic energy*, which measures

the regularity of the deformation ϕ , whereas the second term measures the dissimilarity between the end-point image $I_1 = I_0 \circ \phi_1^{-1}$ and the target image T . The LDDMM image registration objective is to minimize the energy functional E over all deformations. Figure 2 illustrates image registration between two brain MR-slices.

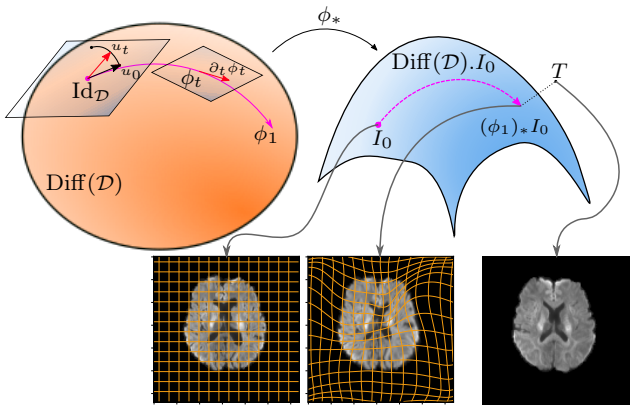


Fig. 2: An illustration of the deformation $t \mapsto \phi_t \in \text{Diff}(\mathcal{D})$ acting on the brain MR-slice I_0 . The deformation transforms I_0 into an image $I_1 = (\phi_1)_*I_0$ being close to T , while also maintaining a low kinetic energy determined from its speed $\|u_t\|$. Observe for example that the lateral ventricles are contracted from I_0 to I_1 to be more reminiscent of those in T .

2.1 The EPDiff Equation

Using calculus of variations on optimal deformations results in a geodesic equation known as the *Euler-Poincaré equation*:

$$\partial_t m_t + \text{ad}_{u_t}^* m_t = 0, \quad m_t = Lu_t. \quad (3)$$

Here $\text{ad}^*: \mathfrak{X}(\mathcal{D}) \times \mathfrak{X}^*(\mathcal{D}) \rightarrow \mathfrak{X}^*(\mathcal{D})$ is the coadjoint action of the diffeomorphism group $\text{Diff}(\mathcal{D})$, and $m = Lu$ is referred to as the *conjugate momentum* associated to the velocity field u . Sometimes the conjugate momentum is defined as $m = \langle Lu, \cdot \rangle_{L^2(\mathcal{D}, \mathbb{R}^3)}$ instead so that it is in fact a dual vector in the classical sense. However, when the conjugate momentum is considered as a map $m = Lu: \mathcal{D} \rightarrow \mathbb{R}^d$, the Euler-Poincaré equation can be written as the *EPDiff equation*

$$\partial_t m_t + Dm_t \cdot u_t + (Du_t)^T \cdot m_t + \text{div}(u_t) m_t = 0, \quad (4)$$

where the relation $m_t = Lu_t$ is implicit. Given an optimal initial momentum m_0 , the EPDiff equation may be solved to recover the entire path of velocities $(u_t)_{t \in [0,1]}$

and hence also the optimal deformation $(\phi_t)_{t \in [0,1]}$ via the reconstruction equation. Optimizing the energy E with respect to m_0 is known as image registration by shooting method.

Instead of first computing the deformation ϕ_t from the reconstruction equation, the induced path of images I_t may be also computed directly from the velocities u_t due to the *image advection equation*

$$\partial_t I_t = -u_t \cdot \nabla I_t. \quad (5)$$

In practice the operator $L: \mathfrak{X}(\mathcal{D}) \rightarrow \mathfrak{X}^*(\mathcal{D})$ is specified from its Green's Kernel $K: \mathcal{D} \times \mathcal{D} \rightarrow \mathbb{R}^d$ given by $LK(\cdot, y) = \delta(\cdot - y)$ where δ is the Dirac distribution and where L acts on the first coordinate of K . For spatially invariant kernels of the form $K(x, y) = k(x - y)\mathbf{1}_d$, for some $k: \mathcal{D}^2 \rightarrow \mathbb{R}$, it is related to L by $L^{-1}m = k * m$, where $*$ denotes convolution. For the simulation studies introduced later, a multi-Gaussian kernel of the form $k(x) = \sum_{i=1}^n w_i \exp(-x^2/\sigma_i^2)$ was used in accordance with [12].

2.2 Perturbing the Reconstruction Equation

To account for random variations in deformations, we now describe the stochastic framework proposed in [2].

Let $\sigma_1, \dots, \sigma_p \in \mathfrak{X}(\mathcal{D})$ be a collection of vector fields which we refer to as *noise fields*. Furthermore, let $W = (W_t^\alpha)_{t \in [0,1]}^{\alpha=1, \dots, p}$ be a p -dimensional Wiener process defined on a universal background probability space (Ω, \mathcal{F}, P) and with independent components $W^\alpha = (W_t^\alpha)_{t \geq 0}$.

The framework is derived from perturbing the flow of the time-dependent vector field $t \mapsto u_t$, which is done by replacing the reconstruction equation (1) with the Stratonovich SDE:

$$d\phi_t(x) = u_t(\phi_t(x))dt + \sum_{\alpha=1}^p \sigma_\alpha(\phi_t(x)) \circ dW_t^\alpha, \quad (6)$$

parametrized over $x \in \mathcal{D}$. Note that $\circ dW_t^\alpha$ denotes the Stratonovich increment, not to be confused with functional composition. The deformation (ϕ_t) is thus a time-continuous stochastic process on $\text{Diff}(\mathcal{D})$. Another view is that ϕ_t follows the reconstruction equation (1), but with the guiding velocity field u_t replaced by the perturbed velocity field \tilde{u}_t given by

$$d\tilde{u}_t = u_t dt + \sum_{\alpha=1}^p \sigma_\alpha \circ dW_t^\alpha. \quad (7)$$

We proceed as before and define the perturbed energy functional \tilde{E} by the same expression as in (2), but where ϕ_1 is obtained from the perturbed reconstruction equation (6) instead.

Consider now a stochastic time-dependent vector field $u: [0, 1] \times \Omega \rightarrow \mathfrak{X}(\mathcal{D})$ such that for each realization $\omega \in \Omega$ it defines a continuous path $t \mapsto u_t = u_t(\omega)$ of vector fields and assume that (P -a.s.) u_t is a critical point of the perturbed energy \tilde{E} . It is then argued in [2], based on the calculations of [7], that the geodesic motion is given by the *stochastic Euler-Poincaré equation*:

$$dm_t + \text{ad}_{u_t}^* m_t dt + \sum_{\alpha=1}^p \text{ad}_{\sigma_\alpha}^* u_t \circ W_t^\alpha = 0. \quad (8)$$

In this new setting the vector field u_t becomes stochastic because we demand that it is a pathwise critical point of the stochastic functional \tilde{E} .

2.3 Stochastic EPDiff and Advection

The explicit expression for the coadjoint action $\text{ad}_{\sigma_\alpha}^*$ on the diffeomorphism group $\text{Diff}(\mathcal{D})$ can be applied on the stochastic Euler-Poincaré equation (8) to obtain the *stochastic EPDiff equation*:

$$dm_t = - (Dm_t \cdot u_t + (Du_t)^T \cdot m_t + \text{div}(u_t)m_t) dt - (Dm_t \cdot \sigma_\alpha + (D\sigma_\alpha)^T \cdot m_t + \text{div}(\sigma_\alpha)m_t) \circ dW_t^\alpha. \quad (9)$$

Note that we have resorted to the Einstein summation convention on the index $\alpha = 1, \dots, p$ for convenience. This equation describes the motion of the velocity u_t and the momentum m_t of a perturbed geodesic motion on $\text{Diff}(\mathcal{D})$. Since the Stratonovich noise is added linearly to the reconstruction equation, and since the advection equation is also linear in u_t , the resulting dynamics of the image evolution is given by the *stochastic advection equation*

$$dI_t = -\nabla I_t \cdot u_t dt - (\nabla I_t \cdot \sigma_\alpha) \circ dW_t^\alpha. \quad (10)$$

See also [1, Equation 3.4] for a derivation based on the stochastic Lie derivative. In the following we refer to the stochastic EPDiff (9) and the stochastic advection equation (10) collectively as the *SEFDA* equations.

If desired, we may consider the SEFDA equations (9, 10) as a starting point of the stochastic shape framework of [2] specialized to images. Figure 1 illustrates different sample realizations of the dynamics defined by the SEFDA equations, with the initial image I_0 being a brain MR-slice.

3 Parameter Estimation

A priori the SEFDA equations define a non-parametric model for stochastic image deformation in the sense that there is an infinite-dimensional freedom in the choice of noise fields. A particular parametric submodel can be specified by parametrizing the noise fields $\sigma_1, \dots, \sigma_p$, i.e., specifying a map of the form:

$$\begin{aligned} \Sigma: \Theta &\longrightarrow \mathfrak{X}(\mathcal{D})^p, \\ \theta &\longmapsto \Sigma(\theta) = (\sigma_1(\theta), \dots, \sigma_p(\theta)), \end{aligned} \quad (11)$$

where $\theta \in \Theta \subseteq \mathbb{R}^q$ is the *noise field parameter*. Note that p is considered as a hyperparameter for simplicity. To infer the noise field parameter we proceed with the method of moments.

3.1 Moment Equations

Let $(m_t, I_t)_{0 \leq t \leq 1}$ be solutions to the SEFDA equations (9, 10). The moment of a stochastic process of maps on \mathcal{D} is defined pointwise and denoted by $\langle \cdot \rangle$, e.g.,

$$\langle m_t \rangle: \mathcal{D} \longrightarrow \mathbb{R}^d, \quad x \mapsto \langle m_t \rangle(x) := \mathbb{E}m_t(x), \quad (12)$$

$$\langle I_t \rangle: \mathcal{D} \longrightarrow \mathbb{R}, \quad x \mapsto \langle I_t \rangle(x) := \mathbb{E}I_t(x). \quad (13)$$

To compute the moments, we reformulate the SEFDA equations as Itô SDE's such that the noise terms vanish in expectation. We briefly summarize the conversion in a general setting.

Let $W = (W_t^\alpha)_{t \in [0,1]}^{\alpha=1, \dots, p}$ be a p -dimensional Wiener process, let $a: \mathbb{R}^n \rightarrow \mathbb{R}^n$ and let $b = (b_\alpha): \mathbb{R}^n \rightarrow \mathbb{R}^{n \times p}$ with $b_\alpha: \mathbb{R}^n \rightarrow \mathbb{R}^n$. Then with sufficient regularity conditions on a and b , an n -dimensional stochastic process $X = (X_t)$ is a solution to the Stratonovich SDE

$$dX_t = a(X_t)dt + b(X_t) \circ dW_t$$

if and only if it is a solution the Itô SDE

$$dX_t = [a(X_t) + \frac{1}{2}c(X_t)]dt + b(X_t) \cdot dW_t,$$

where the term $\frac{1}{2}c(X_t)$ is the *Itô-Stratonovich correction term* given by

$$c(x) = \sum_{\alpha=1}^p Db_\alpha(x) \cdot b_\alpha(x). \quad (14)$$

See for instance [13]. Consider the special case where each $b_\alpha(x) = B_\alpha \cdot x$ is a linear map with $B_\alpha \in \mathbb{R}^{n \times n}$. Then the Jacobian $Db_\alpha = B_\alpha$ corresponds to the linear map itself, and hence the Itô-Stratonovich correction term is $c(x) = \sum_{\alpha=1}^p Db_\alpha(x) \cdot b_\alpha(x) = \sum_{\alpha=1}^p b_\alpha(B_\alpha(x))$.

When the SDE is replaced by an SPDE, the Itô-Stratonovich correction term is formally the same as

(14), but the derivative D should be interpreted as a Fréchet derivative as b is an operator on a normed function space in this case. See [6, Section 4.5.2] for a derivation. Since the coadjoint operator $\text{ad}_{\sigma_\alpha}^* : \mathfrak{X}^*(\mathcal{D}) \rightarrow \mathfrak{X}^*(\mathcal{D})$ and the *fundamental vector fields*

$$\zeta_{\sigma_\alpha} : \mathcal{I}(\mathcal{D}) \longrightarrow \mathcal{I}(\mathcal{D}), \quad I \longmapsto \nabla I \cdot \sigma_\alpha, \quad (15)$$

are linear maps of normed spaces, their Fréchet derivatives are equal to the maps themselves. Hence the Itô-Stratonovich correction terms of the SEPDA equations (9, 10) are

$$\begin{aligned} c_{\text{EPDiff}}(m_t) &= \sum_{\alpha=1}^p \text{ad}_{\sigma_\alpha}^* (\text{ad}_{\sigma_\alpha}^* m_t), \\ c_{\text{Advect}}(I_t) &= \sum_{\alpha=1}^p \zeta_{\sigma_\alpha} (\zeta_{\sigma_\alpha} (I_t)) = \sum_{\alpha=1}^p \nabla (\nabla I_t \cdot \sigma_\alpha) \cdot \sigma_\alpha. \end{aligned} \quad (16)$$

Note that (16) can be written explicitly using the EPDiff expression for the coadjoint operator. The corresponding Itô formulations of the SEPDA equations are therefore

$$\begin{aligned} dm_t &= \left[-\text{ad}_{u_t}^* m_t + \frac{1}{2} \sum_{\alpha=1}^p \text{ad}_{\sigma_\alpha}^* (\text{ad}_{\sigma_\alpha}^* m_t) \right] dt + \text{Itô noise}, \\ dI_t &= \left[-\nabla I_t \cdot u_t + \frac{1}{2} \sum_{\alpha=1}^p \nabla (\nabla I_t \cdot \sigma_\alpha) \cdot \sigma_\alpha \right] dt + \text{Itô noise}. \end{aligned} \quad (17)$$

Now using the fact that the Itô noise vanishes in expectation, combined with the linearity of expectation and $\text{ad}_{\sigma_\alpha}^*$ and ζ_{σ_α} , we obtain the following system of moment equations:

$$\begin{aligned} \partial_t \langle m_t \rangle &= -\langle \text{ad}_{u_t}^* m_t \rangle + \frac{1}{2} \sum_{\alpha=1}^p \text{ad}_{\sigma_\alpha}^* (\text{ad}_{\sigma_\alpha}^* \langle m_t \rangle), \\ \partial_t \langle I_t \rangle &= -\langle \nabla I_t \cdot u_t \rangle + \frac{1}{2} \sum_{\alpha=1}^p \nabla (\nabla \langle I_t \rangle \cdot \sigma_\alpha) \cdot \sigma_\alpha. \end{aligned} \quad (18)$$

These equations cannot be forward integrated due to the terms $\langle \text{ad}_{u_t}^* m_t \rangle$ and $\langle \nabla I_t \cdot u_t \rangle$ appearing on the right-hand side. We therefore resort to the coarse approximations

$$\begin{aligned} \partial_t \langle m_t \rangle &\approx -\text{ad}_{\langle u_t \rangle}^* \langle m_t \rangle + \frac{1}{2} \sum_{\alpha=1}^p \text{ad}_{\sigma_\alpha}^* (\text{ad}_{\sigma_\alpha}^* \langle m_t \rangle), \\ \partial_t \langle I_t \rangle &\approx -\nabla \langle I_t \rangle \cdot \langle u_t \rangle + \frac{1}{2} \sum_{\alpha=1}^p \nabla (\nabla \langle I_t \rangle \cdot \sigma_\alpha) \cdot \sigma_\alpha. \end{aligned} \quad (19)$$

These approximations rely on replacing the product moments

$$\langle Dm_t \cdot u_t \rangle, \quad \langle (Du_t)^T \cdot m_t \rangle, \quad \langle \text{div}(u_t) m_t \rangle, \quad \langle \nabla I_t \cdot u_t \rangle$$

with the products of each moment. Note that equation (19) can in fact be forward integrated since $\langle u_t \rangle = \langle L^{-1} m_t \rangle = \langle k * m_t \rangle = k * \langle m_t \rangle$ by linearity of convolution.

In [2] the same type of problem was encountered when considering stochastic landmark dynamics. Here the *cluster expansion method* (as described in [8]) was employed to also include second order approximations. A similar approach might be possible in this setting, although the computations are more technical due to the infinite-dimensional nature of the SPDE setting. The inclusion of higher order moments will thus be left as a topic for future research. Furthermore, [9] derived moment equations, however in Fourier space using truncated Fourier expansions.

3.2 Constructing an Estimator

Consider now a parametric model of the noise fields $(\sigma_1(\theta), \dots, \sigma_p(\theta)), \theta \in \Theta$, as in (11). We formulate a general procedure for estimation of an unknown ground truth parameter $\theta_0 \in \Theta$ given a sample $I_1(\omega_1), \dots, I_1(\omega_N)$ of N endpoint images sampled from the SEPDA equations with noise fields $\sigma_1(\theta_0), \dots, \sigma_p(\theta_0)$.

To estimate the endpoint moment $\langle I_1 \rangle(\theta)$ for a given choice of noise fields, let $\widetilde{\langle I_1 \rangle}(\theta)$ denote the endpoint moment image obtained from solving (20) with noise fields $\sigma_1(\theta), \dots, \sigma_p(\theta)$. Then for any similarity measure $d : \mathcal{I}(\mathcal{D}) \times \mathcal{I}(\mathcal{D}) \rightarrow [0, \infty)$ of images, we can construct a corresponding loss function $\ell : \Theta \rightarrow [0, \infty)$ given by

$$\ell(\theta) = d\left(\widetilde{\langle I_1 \rangle}(\theta), \frac{1}{N} \sum_{i=1}^N I_1(\omega_i)\right). \quad (21)$$

As $\ell(\theta)$ compares how similar the approximated moment $\widetilde{\langle I_1 \rangle}(\theta)$ is to the empirical mean of the observed images $\frac{1}{N} \sum_{i=1}^N I_1(\omega_i)$, the difference should be small when $\theta = \theta_0$ since they are both approximations of $\langle I_1 \rangle(\theta_0)$. Thus we are led to define the corresponding moment estimator

$$\hat{\theta} := \arg \min_{\theta \in \Theta} \ell(\theta). \quad (22)$$

This estimator can be computed in practice as an optimization problem.

One reasonable choice for similarity measure is the squared distance $d(I, I') = SSD(I, I') = \|I - I'\|_{L^2}^2$, which is often used for classical image registration. Another reasonable choice comes from the normalized cross-correlation (NCC) given by:

$$NCC(I, I') = \frac{\langle I, I' \rangle_{L^2}}{\|I\|_{L^2} \|I'\|_{L^2}}, \quad I, I' \in \mathcal{I}(\mathcal{D}), \quad (23)$$

which has the corresponding similarity measure given by $d_{NCC} := 1 - NCC^2$. One of the features of this similarity measure is that it is invariant under changes in global pixel intensity.

4 Implementation and Parametric Submodels

Having defined the moment estimator $\hat{\theta}$ in (22), we now turn to the discussion of numerical implementation and the choice of parametric submodel. The discussion will then be used to investigate the performance of $\hat{\theta}$ with simulation studies in the next section.

4.1 Implementation

To conduct the simulation studies an implementation¹ was written based on the preexisting *mermaid* library² (iMagE Registration via autoMAtIc Differentiation). The *mermaid* toolbox contains various image registration methods, including a shooting method based on the EPDiff equation (4) and the image advection equation (5).

To carry out Stratonovich integration, a Heun scheme [14] was implemented into the *mermaid* script. The approximated moment equations (19,20) were implemented similarly to the existing registration models, in particular with the *torchdiffeq* library utilizing the adjoint method for ODE integration [5]. As a consequence, the built-in PyTorch optimizers could be applied to update the parameter θ using less memory. For consistency Adaptive Moment estimation (ADAM) was used for all simulation studies.

The simulations were performed on the brain MR-slices shown in Figure 2. In this case the image domain was discretized as $\tilde{\mathcal{D}} = \{(i, j)/127\}_{0 \leq i, j \leq 127}$, but the implementation is not specific to $\tilde{\mathcal{D}}$. The simulations were conducted with an old i5 processor (1.80GHz \times 4) and thus, with the availability of CUDA in the *mermaid* library, it should be possible to upscale to 3D images in future research.

4.2 Parametric Submodels

The choice of parametric submodel is a question of modeling and not a strict mathematical issue. Most of the parametrizations considered can be described in terms of a lattice of radially symmetric noise fields similarly to [2, 9]. To be more precise, let $k: [0, \infty) \rightarrow [0, \infty)$ be a decreasing function and let $\Lambda = \{\mu_1, \dots, \mu_p\} \subset$

$(0, 1)^2$ be a lattice of p points. Then the corresponding parametrization of the noise fields is of the form

$$\sigma_{lm}(x, y) = \lambda_l k(\|(x, y) - \mu_l\|/\tau) \mathbf{e}_m, \quad (24)$$

for $m = 1, 2$, and $l = 1, \dots, p$, and where $\lambda_1, \dots, \lambda_p$ are amplitude parameters, τ is the width of the noise fields and \mathbf{e}_1 and \mathbf{e}_2 are the standard basis vectors in \mathbb{R}^2 . Thus at each lattice point μ_l there are two corresponding noise fields σ_{l1} and σ_{l2} which are going to contribute with independent driving noises W_t^{l1} and W_t^{l2} . One could also have considered a width parameter τ_l for each noise field, but for simplicity the width was eventually considered as a hyperparameter together with the lattice Λ . At first k was chosen to be a Gaussian kernel $k(x) = (2\pi)^{-1/2} e^{-x^2/2}$ as in [2], and henceforth we refer to noise fields based on the Gaussian kernel as *Gaussian noise fields*. Later the cubic B-spline $k = \beta_3$

$$6\beta_3(x) = (x+2)_+^3 - 4(x+1)_+^3 + 6(x)_+^3 - 4(x-1)_+^3 + (x-2)_+^3,$$

was considered due to its compact support. Here $(\cdot)_+ := \max(\cdot, 0)$ denotes the positive part.

The simulations were initially run with a 3×3 square lattice as in [2, 9], but later extended to 4×4 lattice to get a more uniform cover of the image. Thus an explicit parametrization of a square lattice of Gaussian noise fields is given by

$$\sigma_{ijm}(x, y) = \lambda_{ij} \exp\left(-\frac{1}{2\tau^2} \|(x, y) - \mu_{ij}\|^2\right) \mathbf{e}_m, \quad (25)$$

for $m = 1, 2$, and $1 \leq i, j \leq 4$ and with $\mu_{ij} = (i/5, j/5)$.

To obtain a more uniform cover, the idea of a *hexagonal* (triangular) lattice was also considered. The hexagonal lattice structure leads to the densest packing of congruent circles in the plane, which is suitable since the noise fields are radially symmetric. Moreover, the square lattice does not exploit the fact that the brain MR-slice is concentrated at the center of $(0, 1)^2$. In this view, a symmetrically centered hexagonal lattice of 14 gridpoints, shown in Figure 3, was used.

Another parametrization that was studied was the *sinusoidal noise fields* given by

$$\sigma_{nm\ell}(x, y) = c_{nm} \sin(n\pi x) \sin(m\pi y) \mathbf{e}_\ell, \quad (26)$$

for $n, m = 1, \dots, q$, and $\ell = 1, 2$. The motivation for such noise fields comes from the fact that a sufficiently regular function $f: [0, 1]^2 \rightarrow \mathbb{R}$ with boundary condition $f|_{\partial[0, 1]^2} = 0$ can be written as a sine series:

$$f(x, y) = \sum_{n, m=1}^{\infty} c_{nm} \sin(n\pi x) \sin(m\pi y). \quad (27)$$

¹ <https://github.com/AlexanderChristgau/mermaid>

² <https://github.com/uncbiag/mermaid>

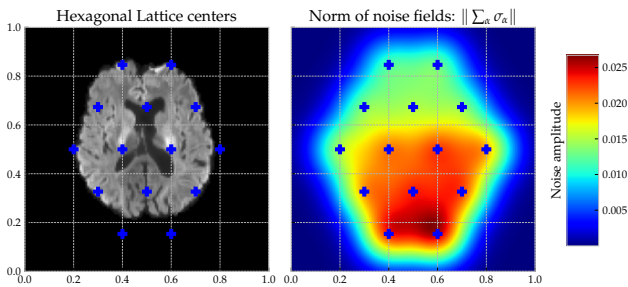


Fig. 3: The left plot shows the hexagonal lattice placed on top of the brain MR-slice. The right plot shows the norm of a particular choice of Gaussian noise fields centered around the hexagonal lattice points.

Other parametric submodels were also tried, e.g. the gradients of the sine basis in view of modeling conservative vector fields. These parametrizations of noise fields did not lead to anything of interest and thus their results are not reported.

5 Results

In this section, we present the results of the following two simulation studies.

Experiment A Here the objective is to test the identifiability of θ for various parametric submodels $\Sigma(\theta)$ using the moment estimator $\hat{\theta}$. The general experimental procedure is therefore:

1. Consider a parametric model $\Sigma(\theta), \theta \in \Theta$, of the noise fields and a ground truth parameter $\theta_0 \in \Theta$.
2. Sample N i.i.d. endpoint images $\{I_1(\omega_i)\}_{i=1, \dots, N}$ by numerically integrating the SEPDA equations with noise fields $\Sigma(\theta_0)$.
3. Estimate θ_0 with the estimator $\hat{\theta}$ by optimizing over $\ell(\theta)$ for the synthetic dataset, and compare $\hat{\theta}$ with θ_0 .

Experiment B Here the objective is to compare the estimated noise fields $\sigma_{\alpha}(\hat{\theta})$ with the ground truth noise fields for a misspecified parametrization $\Sigma(\theta)$. Thus the procedure is the following:

1. Consider ground truth noise fields $\varsigma_1, \dots, \varsigma_{\varrho} \in \mathfrak{X}(\mathcal{D})$ and a parametric model of noise fields $\Sigma(\theta), \theta \in \Theta$, such that $(\varsigma_1, \dots, \varsigma_{\varrho}) \notin \Sigma(\Theta)$.
2. Sample N i.i.d. endpoint images $\{I_1(\omega_i)\}_{i=1, \dots, N}$ from the SEPDA equations with $\varsigma_1, \dots, \varsigma_{\varrho}$ as noise fields.
3. Compute the estimator $\hat{\theta}$ given in (22) from the synthetically sampled dataset and compare $\Sigma(\hat{\theta})$ with $\varsigma_1, \dots, \varsigma_{\varrho}$.

5.1 Experiment A

For the lattice parametrizations, the ground truth amplitudes were chosen such that the resulting noise was on a realistic scale of the brain image, and such that the parameters were spread out, allowing for improved visualization. The ground truth for the Gaussian noise fields was given by lexicographically ordering the lattice points and setting $\lambda_i^{\text{Gauss}} = 0.005 + 0.000625 \cdot (i + 2 \sin i)$. For the cubic B-splines the ground truth was given similarly by $\lambda_i^{\text{B-spline}} = \lambda_i^{\text{Gauss}} / 5$. The kernel width τ was specified as a hyperparameter such that the noise fields had an appropriate overlap. For example, Figure 3 shows the resulting scalar *norm field* $\|\sum_{\alpha} \sigma_{\alpha}\|$ of the ground truth Gaussian hexagonal lattice with $\tau^2 = 0.008$. Otherwise the width was specified as $\tau = 0.15$ and $\tau = 0.1$ for the B-spline noise fields and the Gaussian square lattice, respectively.

For each parametric submodel a dataset of 500 images was sampled by numerically integrating the SEPDA equations with the Heun scheme using 128 equidistant time steps.

Figure 4 shows three random samples and the sample average $\hat{I}_1 := \frac{1}{500} \sum_{i=1}^{500} I_1(\omega_i)$ for a dataset obtained from the Gaussian hexagonal lattice shown in Figure 3. Note that while the variation is subtle, it is greater towards the bottom of the brain in accordance with the specification of the noise fields.

Once each dataset was sampled, the estimator $\hat{\theta}$ from (22) could be obtained by minimizing the loss function $\ell(\theta) = \ell(\lambda_{11}, \dots, \lambda_{44}) = d(\langle \hat{I}_1 \rangle, \hat{I}_1)$. During initial experimentation the NCC-similarity was found to be more effective for parameter estimation, and hence $d = d_{NCC}$ was chosen for all the simulations.

Figure 5 and Figure 7 illustrate the optimization procedures for the Gaussian noise fields and the B-spline noise fields, respectively, both arranged in the hexagonal lattice. The plots are similar, and in both cases the optimization procedure converges towards an accurate estimate of the ground truth after approximately 80 iterations.

The results for the square lattice, shown in Figure 8, were decent but inferior to those of the hexagonal lattice. Observe that estimates of corner amplitude parameters such as λ_{44} are more inaccurate. A reasonable explanation is that noise fields supported outside of the brain are less constrained by the loss function, and thus they may depart from the ground-truth more significantly.

Initially the inclusion of τ^2 as a parameter was also tried and the corresponding results are shown in Figure 10. Observe that the inclusion does not change the relative magnitudes of the amplitude parameters; a

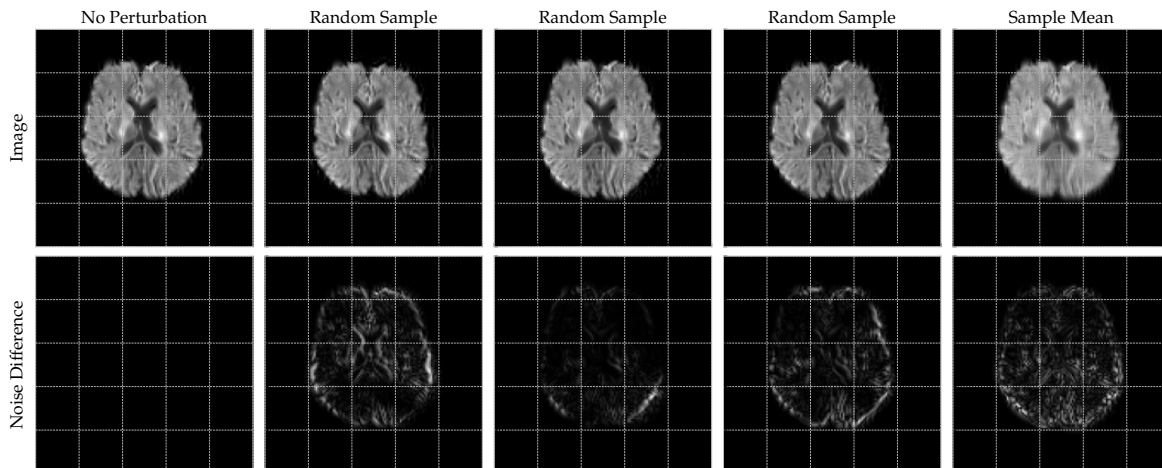


Fig. 4: The rows show the endpoint images and their difference from the deterministic endpoint, respectively, for three random samples and the sample mean of a synthetic dataset sampled from the SEPDA equations. Here the noise fields are Gaussian and arranged in a hexagonal lattice.

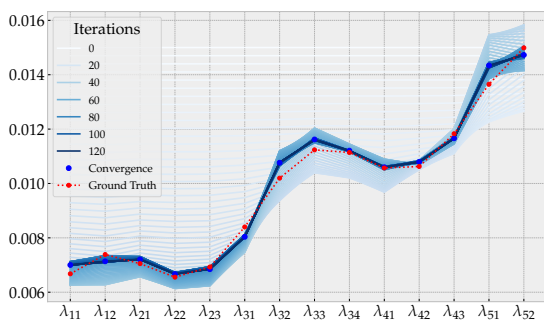


Fig. 5: Parameter inference performed on a dataset generated by the Gaussian hexagonal lattice showing a good convergence towards the ground truth (red).

careful inspection shows that the small overestimation of the width parameter is compensated with a slight underestimation of the amplitude parameters. This is consistent with the fact that both the width and the amplitude govern the total magnitude of the noise. In this view, τ^2 was kept fixed as a hyperparameter for the other experiments.

For the sinusoidal noise fields the ground truth was selected by first considering the function

$$f: (x, y) \mapsto xy^2(1-x)(1-y) \cos(5x) \cos(5y).$$

Then the ground truth was chosen from the sine basis coefficients of f given by

$$c_{nm} = 4 \int_0^1 \int_0^1 f(x, y) \sin(n\pi x) \sin(m\pi y) dx dy,$$

for $1 \leq n, m \leq 4$. The same procedure as in the preceding experiments was followed and the results for the

f -frequencies are found in Figure 9. Note that while the general scale of the estimates seems reasonable, the accuracy of each estimate is poor when compared to the lattice parametrizations. As a consequence, the estimates of the frequency coefficients cannot be used to reconstruct an approximation of the function f .

To end experiment A, Table 1 shows the relative errors of the estimates given by $\|\theta_0 - \hat{\theta}\|/\|\theta_0\|$.

| Parametrization | Relative error |
|--------------------|----------------|
| Gaussian hexagonal | 0.0314 |
| B-spline hexagonal | 0.0262 |
| Gaussian square | 0.0795 |
| Sinusoidal | 0.320 |

Table 1: Relative error $\|\theta_0 - \hat{\theta}\|/\|\theta_0\|$ for various parametric sub-models.

We note that the hexagonal lattice with cubic B-splines provides the most precise estimates, followed by the hexagonal Gaussian noise fields. This is presumably because the compact support of the B-spline leads to less interference between the noise fields. Interference between noise fields may also explain the sinusoidal noise fields poor performance. Inclusion of higher order moments in future research could improve separation of interfering noise fields. We note also that the hexagonal lattice solves the issue of corner noise fields having insufficient overlap, as it was designed for these particular images with a brain placed at the center. For other images containing a different shape, it may be more appropriate with another configuration of noise fields.

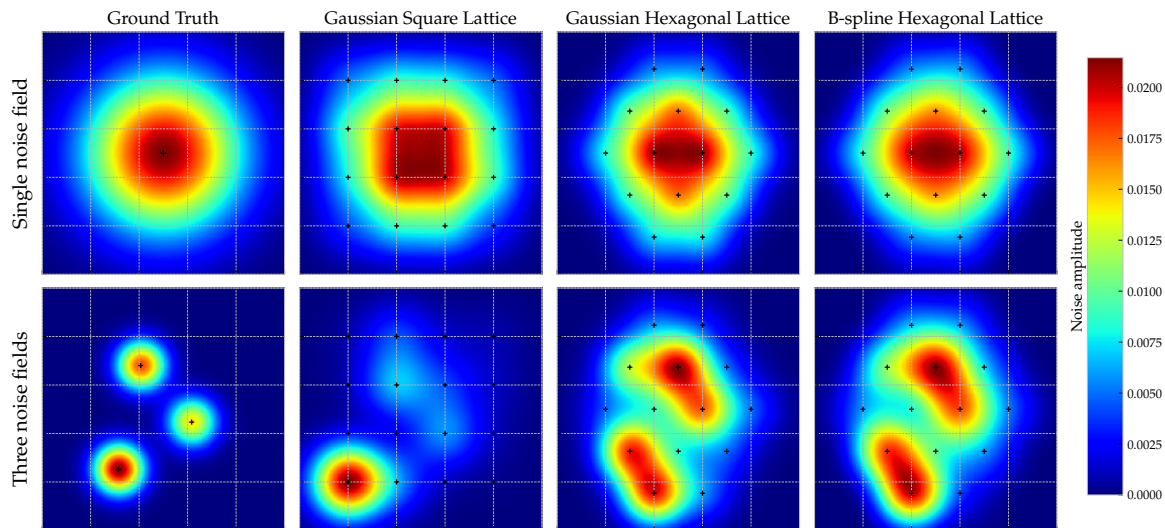


Fig. 6: Noise field inference under model misspecification. The top row shows the models fits onto a single large noise field while the bottom row shows the model fits onto three smaller distinct noise fields.

5.2 Experiment B

The ground truth noise fields used for sampling the synthetic datasets were

1. A single Gaussian noise field placed at the center.
2. Three randomly placed Gaussian noise fields³.

One approach to comparing the fitted noise fields $\Sigma(\hat{\theta})$ with the ground truth noise fields is to display their respective norm fields $\|\sum_{\alpha} \sigma_{\alpha}\|$ perform a visual inspection.

Figure 6 shows the single Gaussian noise field in the top-left subplot and the three distinct Gaussian noise fields in the lower-left subplot. The remaining subplots show the norm fields of the respective models fitted onto a corresponding synthetic dataset of 500 images. We observe that the fitted models visually resemble the ground truth noise fields despite being restricted to their lattice structure with fixed width. For the single noise field the resemblance is clear for all the fitted models and it is ambiguous if any model is better. For the three smaller noise fields the resemblance is slightly less clear. The square lattice overestimates the noise field placed in the lower left and underestimates the two other noise fields, while both of the hexagonal lattice models are unable to separate the noise fields towards the upper right (another visualization of this is given in Figure 11 in the appendix). To get a numerical

³ Their coordinates are (0.617, 0.447), (0.406, 0.681) and (0.314, 0.251).

comparison, consider the quantity

$$SSD \left(\left\| \sum_{\alpha} \sigma_{\alpha}(\hat{\theta}) \right\|, \left\| \sum_{\alpha} \varsigma_{\alpha} \right\| \right), \quad (28)$$

i.e. the squared deviation of the fitted noise fields from the ground truth. Table 2 shows the above quantity for the various fitted models.

| Ground truth | Gauss. sq. | Gauss. hex. | B-spline |
|-----------------|------------|--------------|--------------|
| Single Gaussian | 0.227 | 0.128 | 0.124 |
| Three Gaussian | 1.21 | 0.454 | 0.751 |

Table 2: The similarity between the ground truth and fitted noise fields measured by SSD-similarity (28).

We observe that indeed the single Gaussian noise field is easier to approximate than the three smaller ones. The square lattice yields the worst approximations, which is consistent with the visual inspection and the findings of Experiment A.

In summary, the example in the top row of Figure 6 is well resolved with our choice of noise fields, whereas the bottom row is not. These issues may be dealt with by increasing the density of noise fields, i.e., making the lattices finer or by optimizing the centers of the noise fields in addition to their amplitudes. In an ideal situation, such parametrized noise field positions should adapt to the shape of the noise, but, in practice, they may require repulsion forces between them, with a risk of overfitting.

6 Conclusions and Future Directions

Based on the stochastic generalization of the LDDMM framework introduced in [2], and in particular its specialization to images, we derived the first order moment approximations of the SEPDA equations to construct an estimator for the noise field parameters. With the proposed model for estimation of time-continuous variation in deformations of shapes captured in images, we carried out two main numerical experiments on medical imagery.

In the first experiment, we found that noise field estimators are able to accurately predict the ground truth, provided that the noise fields have sufficient overlap with the content of the image but not too much between themselves, providing indications on when this method works and how to specify noise field locations. In the second experiment, we found that the parametric sub-models are able to approximate some unknown ground truth noise fields, provided there are enough noise fields to resolve the noise structure. This indicates our inference method on noise amplitudes is able to capture any random variation located in the deformation of shapes such as human organs. For such real datasets, the questions of how many noise fields and where to place them on the image may become important for accurate noise estimations while remaining computationally tractable. In particular, one could attempt to optimise for the position and width of all or some of the noise fields to make this method more flexible and with less parameters to set from the users.

Other possible directions for future research include the possibility of time-dependent noise fields for specific applications, other types of profile of noise fields or the use of higher order moment approximations of the SEPDA equations, with e.g. the cluster-expansion approach, to tackle more challenging real world examples, such as longitudinal data extension to 3D images or diffusion tensor imaging.

Acknowledgements AC is grateful to Zhengyang Shen for helpful discussions and guidance for using the `mermaid` library. The work presented is supported by the Villum Foundation grant 00022924, and the Novo Nordisk Foundation grant NNF18OC0052000.

References

- Arnaudon, A., Holm, D., Sommer, S.: String methods for stochastic image and shape matching. *Journal of Mathematical Imaging and Vision* **60**(6), 953–967 (2018)
- Arnaudon, A., Holm, D.D., Sommer, S.: A geometric framework for stochastic shape analysis. *Foundations of Computational Mathematics* **19**(3), 653–701 (2019)
- Bruveris, M., Gay-Balmaz, F., Holm, D.D., Ratiu, T.S.: The momentum map representation of images. *Journal of nonlinear science* **21**(1), 115–150 (2011)
- Bruveris, M., Holm, D.D.: Geometry of image registration: The diffeomorphism group and momentum maps. In: *Geometry, mechanics, and dynamics*, pp. 19–56. Springer (2015)
- Chen, R.T.Q., Rubanova, Y., Bettencourt, J., Duvenaud, D.: Neural ordinary differential equations. *Advances in Neural Information Processing Systems* (2018)
- Duan, J., Wei, W.: *Effective dynamics of stochastic partial differential equations*. Elsevier (2014)
- Holm, D.D.: Variational principles for stochastic fluid dynamics. *Proceedings of the Royal Society A: Mathematical, Physical and Engineering Sciences* **471**(2176), 20140963 (2015)
- Kira, M., Koch, S.W.: *Semiconductor quantum optics*. Cambridge University Press (2011)
- Kühnel, L., Arnaudon, A., Fletcher, T., Sommer, S.: Stochastic image deformation in frequency domain and parameter estimation using moment evolutions. *arXiv preprint arXiv:1812.05537* (2018)
- Marsland, S., Shardlow, T.: Langevin Equations for Landmark Image Registration with Uncertainty. *SIAM Journal on Imaging Sciences* **10**(2), 782–807 (2017). DOI 10.1137/16M1079282
- Miller, M., Banerjee, A., Christensen, G., Joshi, S., Khaneja, N., Grenander, U., Matejic, L.: Statistical methods in computational anatomy. *Statistical Methods in Medical Research* **6**(3), 267–299 (1997). DOI 10.1177/096228029700600305. URL <https://doi.org/10.1177/096228029700600305>. PMID: 9339500
- Niethammer, M., Kwitt, R., Vialard, F.X.: Metric learning for image registration. In: *Proceedings of the IEEE/CVF Conference on Computer Vision and Pattern Recognition*, pp. 8463–8472 (2019)
- Øksendal, B.: *Stochastic Differential Equations: An Introduction with Applications*. Universitext. Springer Berlin Heidelberg (2010). URL <https://books.google.dk/books?id=EQZEAAAQBAJ>
- Platen, E., Bruti-Liberati, N.: Numerical solution of stochastic differential equations with jumps in finance, vol. 64. Springer Science & Business Media (2010)
- Tang, X., Oishi, K., Faria, A.V., Hillis, A.E., Albert, M.S., Mori, S., Miller, M.I.: Bayesian parameter estimation and segmentation in the multi-atlas random orbit model. *PloS one* **8**(6), e65591 (2013)
- Trounev, A., Vialard, F.X.: Shape splines and stochastic shape evolutions: A second order point of view. *Quarterly of Applied Mathematics* **70**(2), 219–251 (2012). DOI 10.1090/S0033-569X-2012-01250-4
- Vialard, F.X.: Extension to infinite dimensions of a stochastic second-order model associated with shape splines. *Stochastic Processes and their Applications* **123**(6), 2110–2157 (2013). DOI 10.1016/j.spa.2013.01.012
- Younes, L.: *Shapes and diffeomorphisms*, vol. 171. Springer (2010)
- Zhang, M., Fletcher, P.T.: Bayesian principal geodesic analysis for estimating intrinsic diffeomorphic image variability. *Medical image analysis* **25**(1), 37–44 (2015)

A Additional Figures and Plots

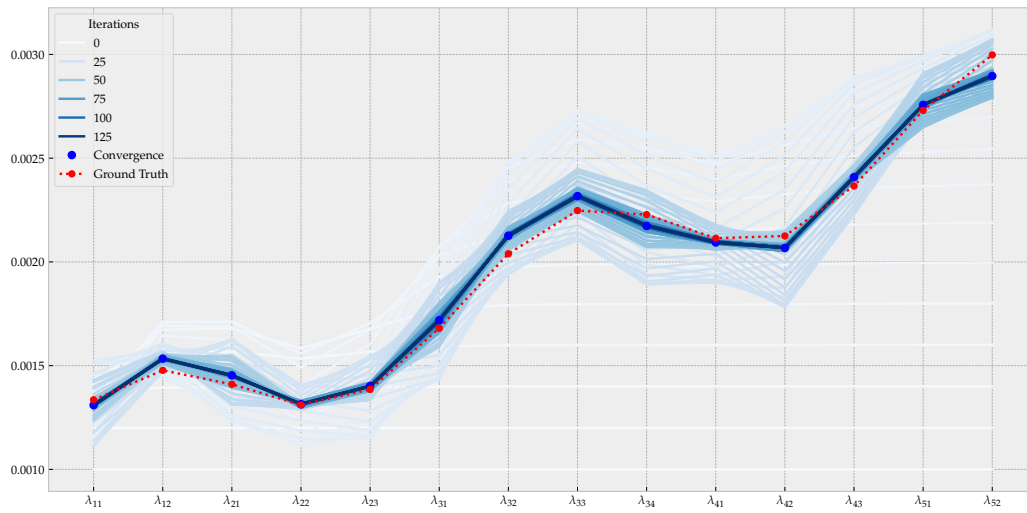


Fig. 7: Parameter inference for data generated by B-splines noise fields.

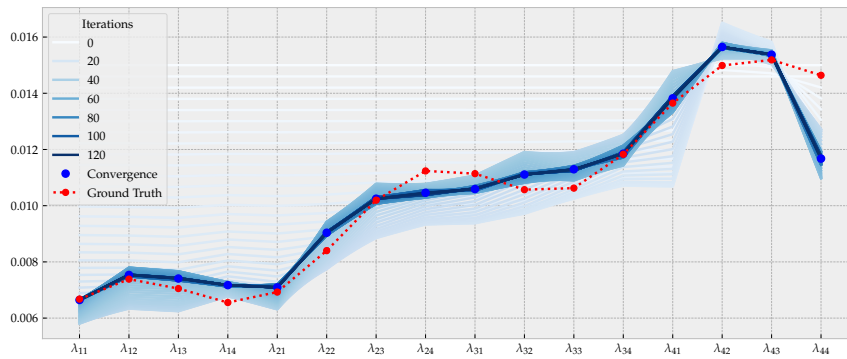


Fig. 8: Optimization procedure of $\ell(\theta) = d(\langle \widehat{I}_1 \rangle, \widehat{I}_1)$ used to infer amplitude parameters λ_{ij} for a 4×4 lattice of Gaussian noise fields, with the width ($\tau^2 = 0.01$) considered as fixed.

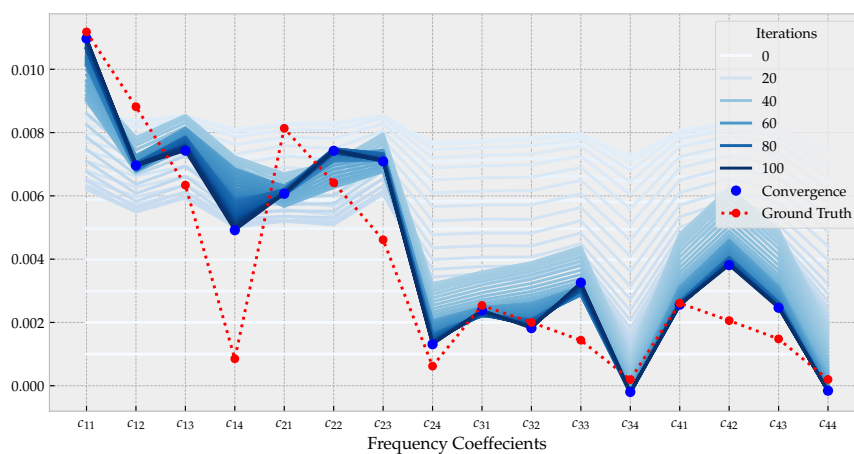


Fig. 9: Inference of frequency coefficients of sinusoidal noise fields.

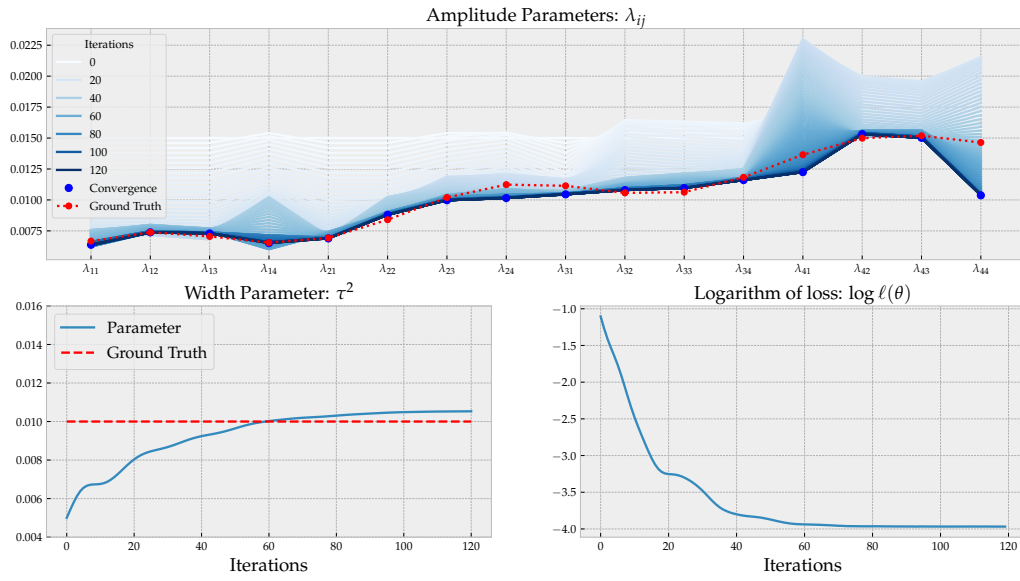


Fig. 10: Optimization procedure of $\ell(\theta) = d(\langle \widehat{I}_1 \rangle, \widehat{I}_1)$ used to infer amplitude parameters λ_{ij} and width parameter τ^2 for a 4×4 lattice of Gaussian noise fields given by (25)

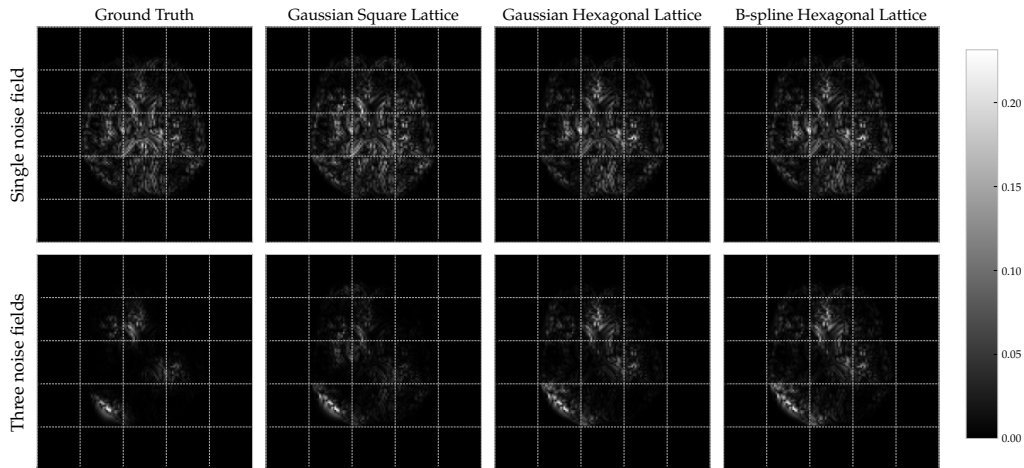


Fig. 11: The first column shows the mean noise difference $|\widehat{I}_1 - I_1^{\text{deterministic}}|$ for the the datasets sampled in Experiment B. The remaining columns show the corresponding predicted mean noise differences $|\langle \widehat{I}_1 \rangle(\widehat{\theta}) - I_1^{\text{deterministic}}|$ for the various model fits.